A PMU-based real-time estimation of voltage stability and margin

Panagiotis Mandoulidis*, Costas Vournas

School of Electrical and Computer Eng., National Technical University of Athens Greece

ARTICLE INFO

ABSTRACT

This paper investigates the performance of New LIVES Index for PMU-based voltage stability monitoring and introduces an on-line local measurement-based voltage stability margin estimation method. Calculations of maximum power transfer, as well as estimation of the error with respect to the long-term voltage instability onset in the presence of system losses are given analytically for a radial system. Simulations on two indicative case studies, namely a radial system and an IEEE test system are used to assess the performance of the above concepts.

1. Introduction

Today's ongoing energy transition, combined with the limited transmission system reinforcements and the variable nature of the ever-increasing renewable energy generation penetration have gradually resulted in operation of Power Systems closer to their capability limits, posing a threat on system Voltage Stability and Security [1,2]. It is well known that stressed system operation can result in blackouts with catastrophic economic consequences [3]. Therefore, on-line Voltage Stability monitoring is still a fundamental factor of Power System Operation and continues to attain great research attention globally.

Instability monitoring can be performed either centralized (using full system model and complete state information) or locally using only available measurements. The centralized approach can estimate the exact voltage instability onset [4,5], however, the complete knowledge of power system state through PMU measurements is still not feasible. On the other hand, real-time decentralized local voltage stability monitoring methods do not rely on system model and they have no need for telecommunications and are thus appropriate for issuing alarms that will help to mitigate and even avoid voltage instability and collapse.

A large part of the early literature on local Voltage Stability on-line monitoring through real-time measurements is based on the impedance matching approach [6–8]. The use of impedance matching theory, however, has certain limitations, such as the assumption of constant load power factor at the point of phasor measurement. In large scale power systems on the other hand, PMU devices at the transmission level monitor relatively wide load areas, where several types of composite loads and distributed generation are connected through a meshed network. In this respect the assumption of constant power factor for the measured load is quite inaccurate and may result in considerable errors, regarding the instability onset detection. Also, the effect of other loads, upstream or in parallel with the monitored part of the system influence the calculated Thevenin equivalent, which is variable and thus does not conform to the impedance matching theorem assumptions. For instance, in Ref. [9] it was shown that in a two-load system impedance matching conditions as monitored on the one load appear long after the instability onset, which depends on both loads.

Even though the exact calculation of instability onset requires knowledge of the complete power system state including generator overexcitation conditions, as explained in Refs. [2,4] and [5], an approximate estimation based exclusively on local measurements is still possible. In order to set up such a problem of approximate decentralized, measurement-based Voltage Instability monitoring, it is useful to define an upstream, as well as a downstream power network. Several research efforts attempt to calculate an equivalent upstream and downstream power system [10,11] relying on PMU measurements, based on which to estimate voltage instability onset.

A good estimation of voltage instability onset for a load area can be provided in real-time, if the boundary buses are monitored through PMU measurements, as shown in Ref. [12], where the sensitivity of transferred active power to apparent conductance is used as an Index. Nonetheless, the following issues remain open:

- The error introduced by power losses downstream from the PMU location has an influence on the instability detection that needs to be assessed.
- A real-time estimation of stability margin i.e. the distance between

---

* Corresponding author.
E-mail addresses: pmandou@power.ece.ntua.gr (P. Mandoulidis), vournas@power.ece.ntua.gr (C. Vournas).
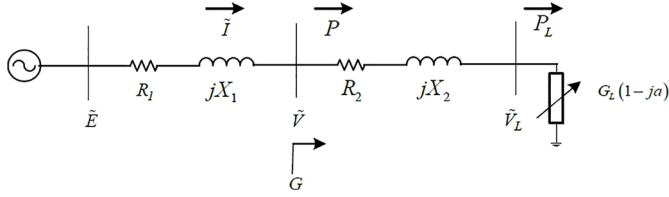
Fig. 1. Radial system with losses and constant power factor load.

measured load power and maximum power transfer is also required.

In this paper two test power systems are utilized to investigate the above considerations. The first one is a simple radial power system and is analysed in detail, so that analytical formulas are extracted. The second one is the IEEE Nordic test System and is simulated in Section 6. The radial system is shown in Fig. 1, where a PMU is assumed to be installed at the intermediate bus between an assumed Thévenin equivalent upstream network and a load bus, fed through a transmission line (downstream network).

The main contribution of this paper with respect to earlier work by the authors [12] is the introduction of a method to estimate the active power (MW) voltage stability margin in real time based solely on measurements taken at a transmission bus, as well as the investigation of the effect of downstream network losses to the maximum power transmitted.

The paper is organised as follows: In Section 2 a short review of the maximum power transfer and impedance matching theorems is presented, along with the voltage stability Index definition and its implementation considerations. The performance of the Index in the radial system in the presence power losses, as well as in the lossless case is analysed in Section 3 by extracting analytical formulas and showing the impact of several different system parameters. In Section 4, the Voltage Stability margin estimation method based on local measurements is presented conceptually, while numerical results for the radial system case study are presented in Section 5 and for the IEEE Nordic test system in Section 6 respectively. Main conclusions and further considerations are summarized in Section 7.

2. Maximum power conditions and Index definition

2.1. Radial test system description

A radial power system with given ideally constant voltage source $\hat{E}$ and equivalent Thévenin impedance is assumed in Fig. 1. The PMU at the intermediate transmission bus measures phasors $\hat{V}$ and $\hat{I}$ and can therefore calculate the apparent downstream impedance, as well as the active and reactive power transferred to the downstream network. It should be noted that the problem of determining an upstream and a downstream network with information from a specific transmission bus may not be an easy task [13]. Two different network configurations are considered, one in which the network is lossless (i.e. $R_1 = R_2 = 0$) and one including losses to highlight their effect.

In both configurations a constant power factor load is assumed, as well as a constant network. The constant power factor load implies that the imaginary part of the admittance $Y_L = G_L + jB_L$ depends on the real part, that is

$$B_L = -\alpha G_L \tag{1}$$

where $a = \tan\varphi$ and $PF = \cos\varphi$ is assumed lagging for $a > 0$.

2.2. Maximum power conditions

For the system in Fig.1 the consumed load active power P_L is:

$$P_L = \frac{G_L(1+\alpha^2)E^2}{[1+(R_1+R_2)G_L(1+\alpha^2)]^2 + [\alpha+(X_1+X_2)G_L(1+\alpha^2)]^2} \tag{2}$$

If $\hat{E}$, line impedances and power factor are all considered constant, then the load active power is a function only of the independent variable G_L. It is well known that maximum power transfer (maxP_L) occurs when the following expression holds for the load admittance, according to the impedance matching theorem [14]:

$$\sqrt{1+\alpha^2}\,G_{L,\max P_L} = \frac{1}{\sqrt{(R_1+R_2)^2+(X_1+X_2)^2}} \tag{3}$$

and the corresponding maximum load power is:

$$\max P_L = \frac{E^2}{2\sqrt{1+\alpha^2}\sqrt{(R_1+R_2)^2+(X_1+X_2)^2}+(R_1+R_2)+\alpha(X_1+X_2)} \tag{4}$$

This impedance matching cannot be directly detected by the PMU at the intermediate bus measuring $\hat{V}$ and $\hat{I}$, because R_2 and X_2 are included in the apparent impedance measured by the PMU. In other words, the PF seen from the intermediate bus is not constant and thus the impedance matching condition does not correspond to maximum power transferred. The actual load impedance is also unknown in general.

2.3. New LIVES Index (NLI)

The voltage stability Index originally presented in Ref. [12] is called New LIVES Index (NLI) and is defined as:

$$NLI = \frac{\Delta P}{\Delta G} \tag{5}$$

where G represents the apparent conductance and P the active power, both as seen from the measuring device, i.e. in this case the PMU at the intermediate bus:

$$G = Re\{\hat{I}/\hat{V}\} \tag{6}$$

and

$$P = Re\{\hat{V}\hat{I}^*\} \tag{7}$$

and ΔP, ΔG refer to the difference between two consecutive measurements of P and G.

In practice, all measured signals are sampled at a constant high sampling rate and contain noise as well as irrelevant information due to short-term system dynamics not related to long-term voltage stability. This complicates the calculation of the NLI Index, as noise is expected to be further amplified when computing differences, such as in (5).

Thus, the same filtering approach as in Ref. [12] has been deployed, which utilizes the Short-Time Fourier Transform (STFT) on calculated G and P signals and generates at discrete time instants t_k (not necessarily equidistant) the piecewize DC signals $G_f(t_k)$ and $P_f(t_k)$. With this notation, NLI is calculated as:

$$NLI_k = \frac{P_f(t_k) - P_f(t_{k-1})}{G_f(t_k) - G_f(t_{k-1})} = \frac{\Delta P_f(t_k)}{\Delta G_f(t_k)} \tag{8}$$

Fig. 2 illustrates the concept of the generated piecewise DC signals from the initial input signals P and G, containing noise.

A new value NLI_k is calculated with (8) only for positive enough increments of G_f and when absolute $\Delta P_f(t_k)$ is greater than a specified threshold, i.e. when the following conditions hold:

$$|\Delta P_f| > \varepsilon \tag{9}$$

$$\Delta G_f > \eta \tag{10}$$

Thus, the NLI responds to load demand growth and not to measurement noise or irrelevant disturbances. Finally, a moving average of the NLI can also be used to further smoothen the effect of sudden changes in a real system at the cost of a small extra delay in issuing the alarm.

In Ref. [12] it is shown, that NLI can monitor exactly voltage instability when the PMU is placed at the load bus, whereas in a general
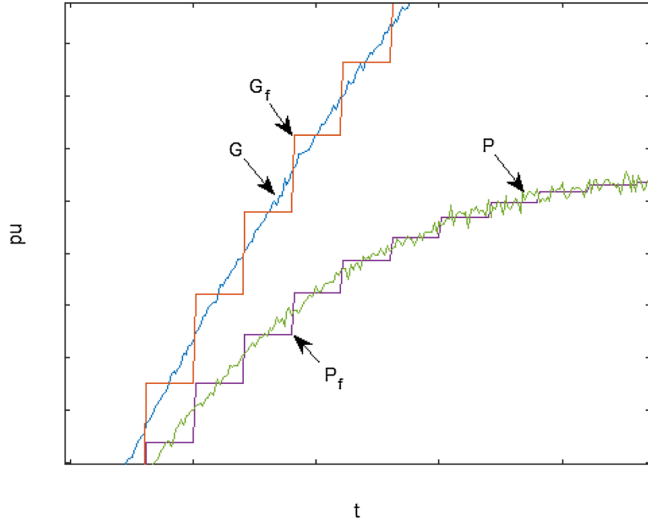
Fig. 2. Apparent conductance, active power and respective filtered signals.

transmission network an approximation is involved. The following Section elaborates on the *NLI* performance in a radial power system, considering the effects of power losses.

3. Effect of losses on NLI performance

3.1. Lossless radial system

In the lossless radial system ($R_1 = R_2 = 0$) the apparent load conductance as seen from the PMU bus is the following function of the load conductance G_L:

$$G = Re\{\hat{I}/\hat{V}\} = \frac{G_L(1 + \alpha^2)}{1 + [a + X_2 G_L(1 + \alpha^2)]^2} \tag{11}$$

At the point of maximum power transfer the Index defined in (8) switches from positive to negative values, while G_L increases [12]. This holds because after the maximum power transfer the transmitted power $P = P_L$ starts to decrease, while the apparent conductance continues to increase. The following relation between the load conductance at maximum power $G_{L,maxP}$ and at maximum apparent conductance $G_{L,maxG}$ ensures that the *NLI* changes sign exactly at the point of maximum power transfer (voltage stability limit) in this case:

$$G_{L,maxP} = G_{L,maxP_L} = \frac{1}{\sqrt{1 + \alpha^2}(X_1 + X_2)} < \frac{1}{\sqrt{1 + \alpha^2}X_2} = G_{L,maxG} \tag{12}$$

3.2. Radial network with losses

If transmission losses are considered it is obvious that P exceeds P_L and will thus reach maximum at a different operating point than P_L. The apparent conductance measured at the PMU transmission bus is given as the following function of load conductance:

$$G = Re\{\hat{I}/\hat{V}\} = \frac{G_L(1 + \alpha^2)[1 + R_2 G_L(1 + \alpha^2)]}{[1 + R_2 G_L(1 + \alpha^2)]^2 + [a + X_2 G_L(1 + \alpha^2)]^2} \tag{13}$$

The load conductance value corresponding to the maximum of (13) is:

$$G_{L,maxG} = \frac{1}{\sqrt{1 + \alpha^2}(X_2 - aR_2) - (1 + \alpha^2)R_2} \tag{14}$$

The load consumed active power was given in (2), while the transmitted active power measured by the PMU is given the following expression respectively:

$$P = \frac{G_L(1 + \alpha^2)[1 + R_2 G_L(1 + \alpha^2)]E^2}{[1 + (R_1 + R_2)G_L(1 + \alpha^2)]^2 + [a + (X_1 + X_2)G_L(1 + \alpha^2)]^2} \tag{15}$$

If E, X_1, X_2, R_1, R_2 and φ are constant, P_L and P are both functions only of G_L. At the maximum of P_L condition (3) holds, while (15) is maximized for the following value of load conductance:

$$G_{L,maxP} = \frac{1}{\sqrt{1 + \alpha^2}\sqrt{R_1^2 + (X_1 + X_2 - aR_2)^2} - (1 + \alpha^2)R_2} \tag{16}$$

Clearly the impedance matching condition holds only for the load power, while the measured transmitted power is maximized at a different value of load conductance.

From (14) and (16) it follows that for $X_1 > 0$ and $R_1 > 0$:

$$G_{L,maxP} < G_{L,maxG} \tag{17}$$

which means that the apparent conductance G continues to increase with load G_L, even after the point of maximum power transfer max$P$.

On the other hand, comparison of (3) and (16) shows that for $R_2 > 0$, P is maximized after P_L when the following condition holds:

$$-(R_1 + R_2) - a(X_1 + X_2) < \sqrt{1 + a^2}\sqrt{(R_1 + R_2)^2 + (X_1 + X_2)^2}$$

which in turn can be proven to hold for all *PFs*. This leads to the generalized conclusion that for the radial system case of Fig. 1:

$$G_{L,maxP_L} \le G_{L,maxP} \tag{18}$$

with the equality holding for $R_2 = 0$, as already discussed.

Thus, in the presence of downstream losses *NLI* becomes negative at the point of max$P$ which occurs after maxP_L for increasing load conductance, in other words it issues a delayed instability alarm. The difference between load conductance for the maximum measured power and the load conductance corresponding to maximum load power is a measure of this discrepancy:

$$\Delta G_M = G_{L,maxP} - G_{L,maxP_L} \ge 0 \tag{19}$$

The delay of the voltage instability onset due to line resistance can be quantified (in per cent) as:

$$e = \frac{\Delta G_M}{G_{L,maxP_L}} \tag{20}$$

4. Voltage stability margin estimation

The voltage stability margin estimation method proposed here is based on local measurements at the PMU bus and makes usage of the *NLI* Index. The main idea is to use the available P and G measurements to generate interpolating polynomials, which estimate the power transfer trend, and thus the maximum power transfer to the downstream network.

Consider the following three pairs of filtered signals G_f and P_f as described in Section 2.3. For every three successive *NLI* calculations ending at t_k, we define the following pairs:

$$[G_0, P_0] = [G_f(t_{k-2}), P_f(t_{k-2})] \tag{21}$$

$$[G_1, P_1] = [G_f(t_{k-1}), P_f(t_{k-1})] \tag{22}$$

$$[G_2, P_2] = [G_f(t_k), P_f(t_k)] \tag{23}$$

An interpolation polynomial of the second order is calculated when the following conditions hold:

$$\Delta P_f(t_k) > \varepsilon \, \Delta P_f(t_{k-1}) > \varepsilon \tag{24}$$

$$NLI_k - NLI_{k-1} < 0 \tag{25}$$

i.e. when for two consecutive time instants there is an increase of active power transfer P_f and a decrease of the corresponding *NLI*. The maximum value of the interpolating function estimates the voltage stability

(maximum power) limit. An apparent conductance increase is implied anyway during the time interval $[t_{k-2}, t_k]$, because otherwise ΔP_f (and NLI_k) would not have been calculated at the corresponding time instants.

The interpolating function is a second-degree Lagrange polynomial [15] calculated at time t_k:

$$p_k(G) = \sum_{j=0}^{2} P_j L_{2,j}(G) \tag{26}$$

Function $L_{2,j}(G)$ is a second degree polynomial corresponding to the pair $[G_j, P_j]$ and has the property that $L_{2,j}(G_i) = 0$ when $i \neq j$ and $L_{2,j}(G_i) = 1$ when $i = j$, thus in the general case of n-degree-polynomial (corresponding to $n + 1$ pairs $[G_0, P_0] - [G_n, P_n]$) it is:

$$L_{n,j}(G) = \frac{[G - G_0]...[G - G_{j-1}][G - G_{j+1}]...[G - G_n]}{[G_j - G_0]...[G_j - G_{j-1}][G_j - G_{j+1}]...[G_j - G_n]} \tag{27}$$

Conditions (24) and (25) guarantee that the second order polynomial will have a maximum for $G > G_2$.

We define the maximum value attained by the interpolating polynomial $p_k(G)$ with the following notation:

$$\hat{P}(t_k) = \max p_k(G) \tag{28}$$

The estimated margin P_M at time t_k is calculated according to the following expression:

$$P_M(t_k) = \hat{P}(t_k) - P_f(t_k) \tag{29}$$

5. Numerical results (radial system)

For the purposes of assessing the performance of *NLI* and the margin estimation method, two case studies are presented, each one with distinct characteristics, namely a radial system in this Section and the Nordic IEEE Test-System [16] in the next one. Since in the radial system case analytical formulas are extracted, both ΔG_M and e are calculated.

5.1. Radial system data

In the radial system of Fig. 1 two sub-cases are considered, namely one where the system is lossless and no measurement noise is incorporated, and one where losses are included and where noise is superimposed in the PMU measurements. The lossless radial case focuses on the exact instability onset identification by the *NLI*, while the one with losses on the approximation error and the effect of noise on PMU measurements.

In the second radial system case both measurements of $\hat{V}$ and $\hat{I}$ are assumed to contain Gaussian noise, in the form of an associated superimposed phasor. Thus, each measured by the PMU current and voltage phasor is assumed to be of the following form:

$$\hat{V}_{measured} = \hat{V}(1 + me^{j\theta}) \tag{30}$$

where m and θ are random numbers. Parameter m follows a normal distribution with standard deviation σ and mean value μ, while parameter θ uniform distribution in [0°, 360°].

In Table 1 the parameters for the two radial network cases are presented. The left column of Table 1 lists the common radial network parameters, while the right column the additional ones of the case including losses. Values for parameters μ and σ of random variable m are shown in Table 2. Table 3 contains the *NLI* thresholds of (9) and (10), whereas the resulting critical apparent conductance values, as well as the corresponding error e for each network case are shown in Table 4.

Both numerical examples of the radial system consider a constant ramp increase of load conductance G_L from zero up to a maximum predetermined value, large enough so that the system exceeds its power transfer limit and long-term voltage instability occurs.

Table 1
Network parameters.

Radial system parameters			
Lossless system		**System with losses**	
E	1.00 pu	R_1	0.05 pu
X_1	0.15 pu	R_2	0.03 pu
X_2	0.20 pu		
Load PF	1.0		

Table 2
Gaussian noise parameters.

Parameter	Value
σ_m	0.033
μ_m	0

Table 3
NLI filtering parameters.

Parameter	value
ε	10^{-4} pu
η	10^{-3} pu

Table 4
Radial system results.

Lossless		With losses	
$G_{L,\max P}$	2.86 pu	$G_{L,\max P}$	3.09 pu
$G_{L,\max P_L}$	2.86 pu	$G_{L,\max P_L}$	2.79 pu
e	0	e	0.11 pu
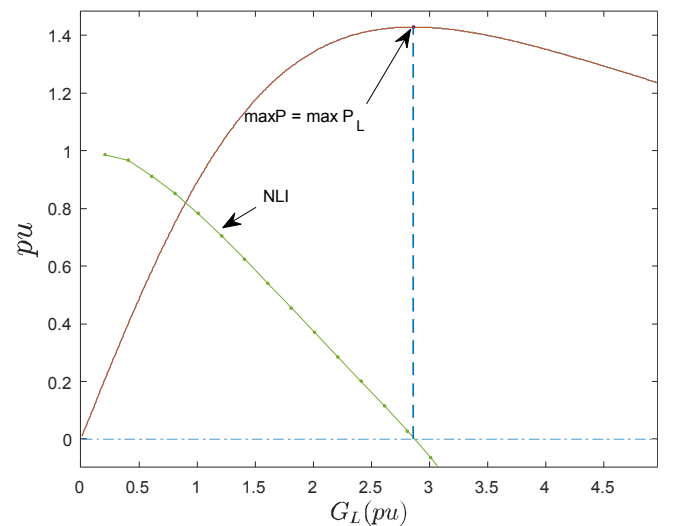
Fig. 3. Lossless case, P_L, P and *NLI* plots.

5.2. Lossless radial system without noise

For the case of the lossless and noiseless radial system, Fig. 3 shows the resultant graphs of $P = P_L$ as a function of load conductance G_L, as well as the calculated *NLI*.

The abscissa of all presented figures is G_L in pu, but if a constant load demand ramp is assumed this is also an indication of time (for the *NLI* calculations). All points where *NLI* is calculated are marked with a dot and between two successive calculations G_L is increased by $0.2\, pu$.

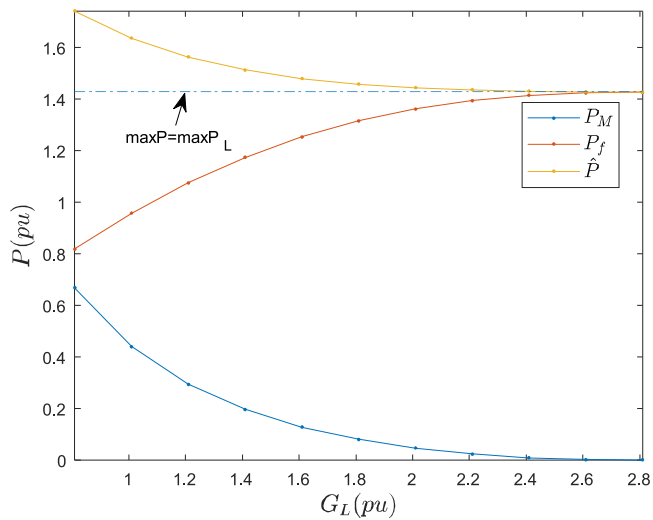As Fig. 3 shows, in the lossless radial case *NLI* becomes negative at

Fig. 4. $\hat{P}$, P_f and margin P_M for lossless case.

Fig. 6. Case with included losses, P_L, P and *NLI* plots.

its first calculation after the onset of instability, as was expected. Since no losses are involved in this case $G_{L,\max P}$ and $G_{L,\max P_L}$ coincide, i.e. the error ΔG_M and percent delay e are both zero.

In Fig.4 the calculated margins during the load increase are shown. As can be seen, the estimated maximum power remains within a band of $0.3\,pu$ and approaches the actual limit maxP_L, as the operating point gradually reaches the instability onset. The estimated maximum active power $\hat{P}$ is the maximum value of each interpolating polynomial, as explained in Eq. (28). It is noted that the last *NLI* calculation on which (24) and (25) hold occurs at approximately $G_L = 2.81\,pu$ a little before the maximum at $G_L = 2.86\,pu$ is reached. After this point no further margin estimations are performed because (24) and (25) cease to hold ($\Delta P_f < 0$).

5.3. Effect of losses and noise

In the second case, noise is included in the measurements of $\hat{I}$ and $\hat{V}$ according to (30). In addition, network losses are nonzero.

In Fig. 5, (3) and (16) are plotted as functions of $a = \tan\varphi$ for the network parameters of Table 1. As seen in the figure, expression (18) is verified also numerically. As discussed, this implies a delayed alarm issued by the *NLI* method, as well as a positive ΔG_M and e.

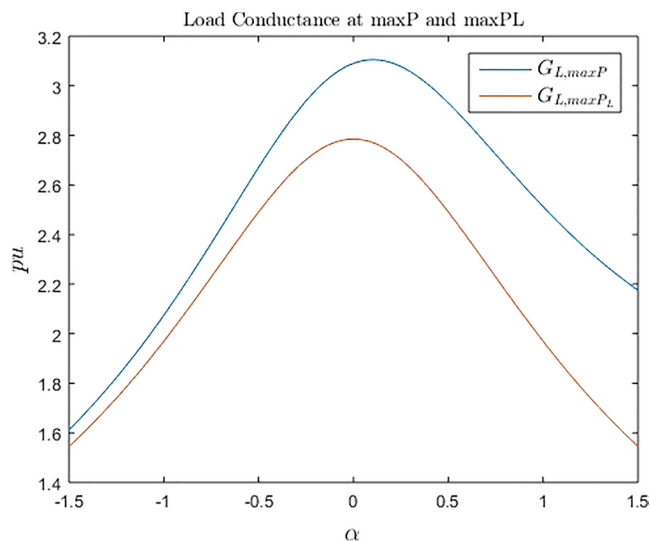Fig. 6 shows the resultant graphs of P and P_L, as well as the

calculated *NLI*. The *NLI* exhibits some fluctuations compared to the previous case without noise and losses, but shows a clear trend towards zero, crossing it slightly after the maximum power transfer. The delayed zero crossing by the *NLI* (occurs at max$P$, after maxP_L) is explained by (18).

In Fig. 6, $G_{L,\max P}$ is seen to be somewhat different compared to the one in Table 4. The discrepancy occurs due to the noise added to the measurements of $\hat{I}$ and $\hat{V}$, while the calculated value in Table 4 is derived from (3). In Fig. 7 the calculated margins are presented.

All estimated maximum power values remain within a band of $0.2\,pu$ and they gradually approach the maximum transmitted active power max$P$. The effect of noise in the PMU measurements is reflected on the slight fluctuations of the estimated margins. The corresponding max$P$ value in Fig. 7 has been computed numerically by using the MATLAB max function. It corresponds to the maximum measured value of the PMU and thus includes noise, which has an impact on the maximum measured value. This value differs slightly from the one that would have been obtained by maximizing (15) with respect to G_L.

From the corresponding figures it is evident that despite the slight discrepancy with respect to the maximum estimated transmitted active power due to the noise and downstream network losses, a relatively accurate margin estimation in terms of active power is timely calculated for the case of a simple radial system
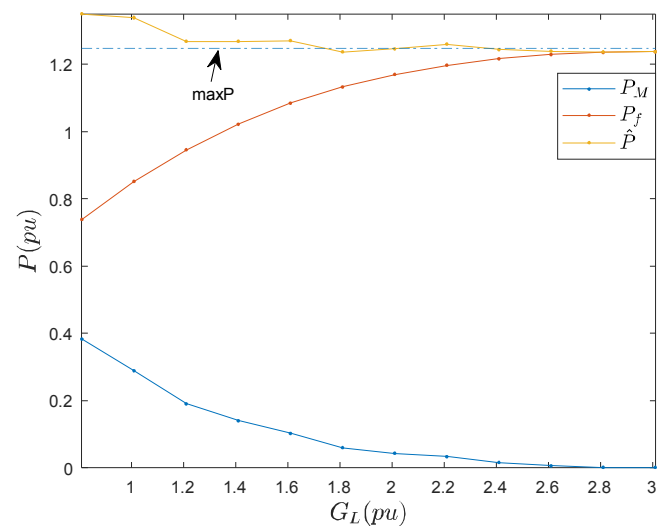

Fig. 5. Graphs of $G_{L,\max P}$ and $G_{L,\max P_L}$ for leading and lagging *PF*.

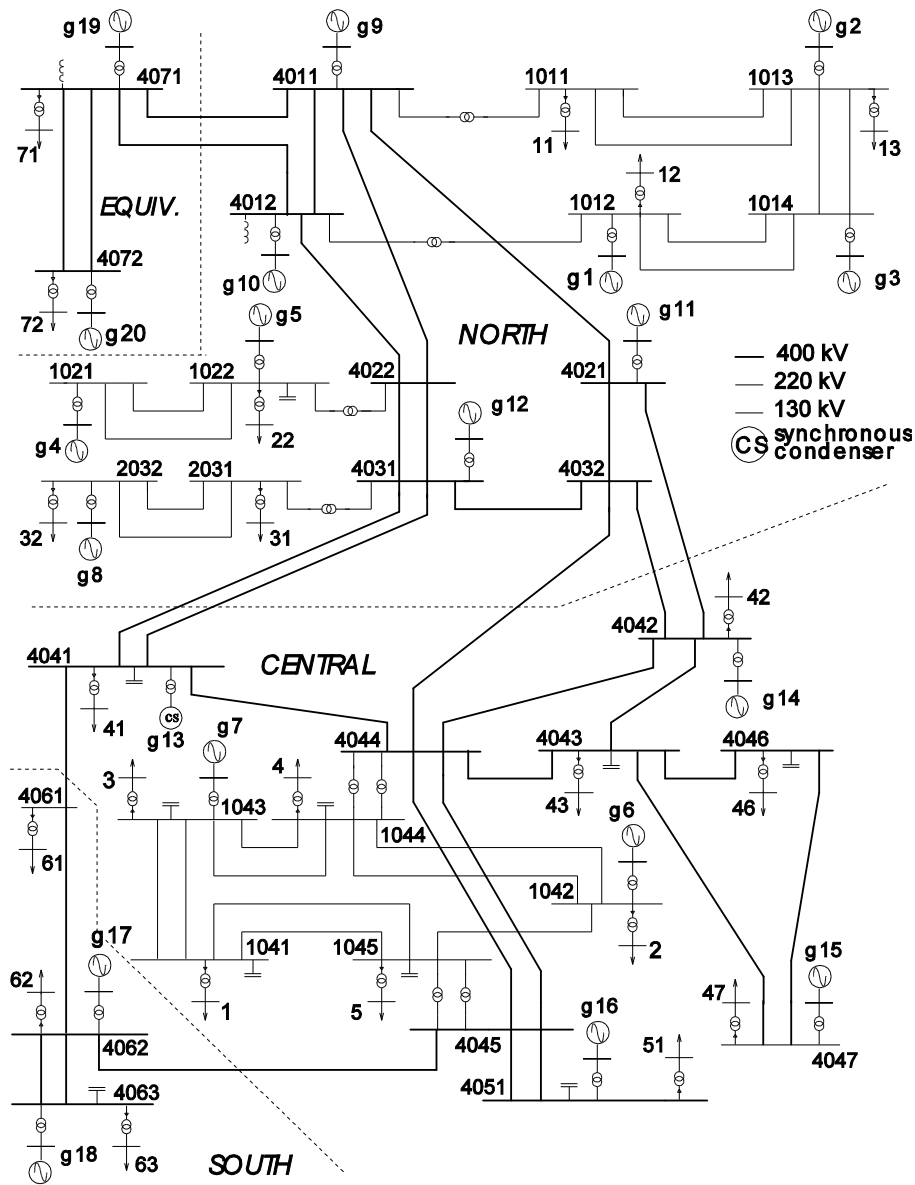**Fig. 7.** Estimated maximum active power $\hat{P}_{\max}$ and margin ΔP with losses.

Fig. 8. IEEE Nordic Test System.

In addition, when applying *NLI*, as well as the margin calculation method in a meshed power system, as in the following section, the delay ΔG_M, as shown previously in Fig. 6, in predicting the instability onset, and the resulting over-estimation of margin, as shown in Fig. 7, is somehow offset by the discrepancy between maximum power transfer in the corridor and the actual instability point, as discussed in [12].

6. Nordic test system

6.1. System description

The performance of the voltage stability margin estimation method is assessed in this Section using the IEEE Nordic test system depicted in Fig. 8. The system is described in full detail in [16] including network data, initial operating points and all controller modelling and data including generator saturation, as well as turbine/governor and AVR systems.

Full-time-scale simulation is performed with RAMSES software developed in the University of Liege [17]. Loads are represented as lumped consumptions at the secondary of HV/MV substations, with a constant current active and constant impedance reactive characteristic.

Load restoration to constant power occurs implicitly through the Load Tap Changers (LTC) at the substation transformers.

The system consists of four areas: (i) the Northern Area, which includes mainly hydro generation; (ii) a simple equivalent external system connected to the North; (iii) the Southern Area which is weakly connected with the rest of the system, and (iv) the Central Area, which constitutes the main consumption area having only a few thermal power plants. The transmission system consists of long 400 kV transmission lines, as well as some 220 and 130 kV lines. The main power transfer corridor is formed by the transmission lines between boundary sending buses 4021, 4031, 4032 and boundary receiving buses 4041, 4042 and 4044, transferring power from the Northern to Central Area. The system can exhibit long-term voltage instability in case there is a corridor line contingency and the system consumption is restored through LTC mechanisms, while reactive power limits are imposed by Overexcitation Limiter (OEL) activation at the generators in Central area.

A PMU is assumed to be installed on each boundary receiving bus, namely on buses 4041, 4042 and 4044, measuring the bus voltage, as well as the corresponding imported current from the transmission corridor lines i.e.:
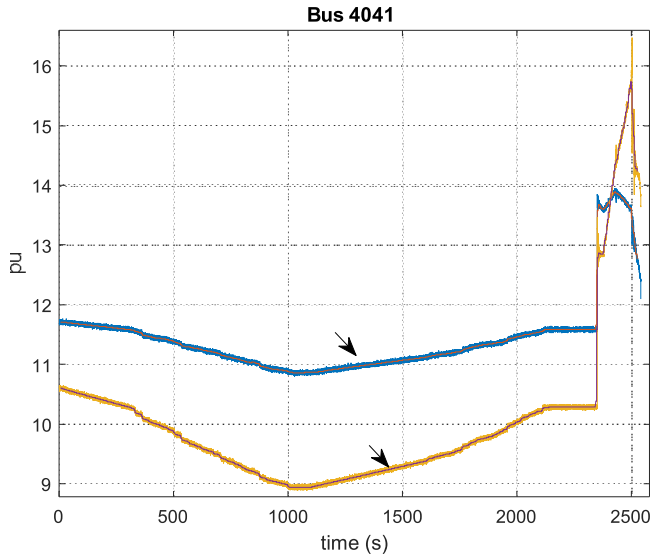
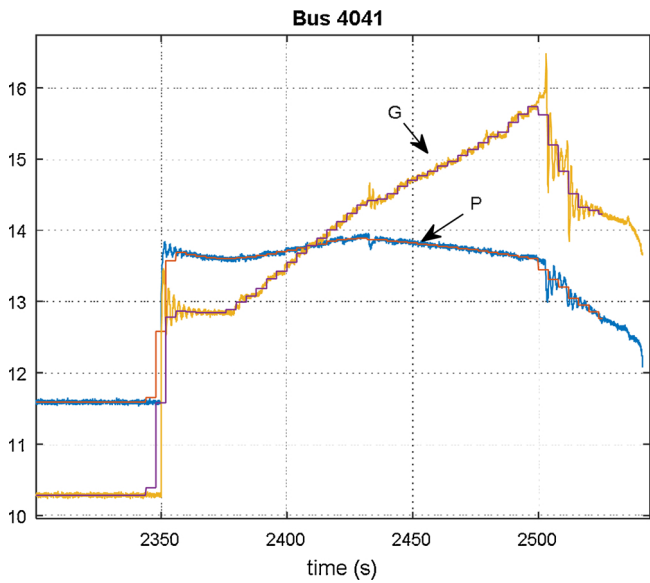**Fig. 9.** Bus 4041 active power and apparent conductance (unstable scenario).

Fig. 10. Bus 4041 active power and apparent conductance during contingency (Unstable case).

$$\hat{I}_i = - \sum_{k \in K_i} \hat{I}_{ik} \tag{31}$$

where K_i is the set of corridor lines connected to receiving boundary bus i.

Each PMU calculates the corresponding incoming active power received by the boundary bus, as well as the apparent conductance of the downstream system. The net incoming power is:

$$P_i = Re\{\hat{V}_i \hat{I}_i^*\} \tag{32}$$

whereas the conductance as seen by each PMU is computed according to (6):

$$G_i = Re\{\hat{I}_i^* / \hat{V}_i\} \tag{33}$$

Two scenarios are simulated, similar with the ones presented in Ref. [16]. As explained in Ref. [16], Scenario A is marginally unstable, while Scenario B is stable. The disturbances for each scenario are identical, but the initial operating point is different as explained in Ref. [16].

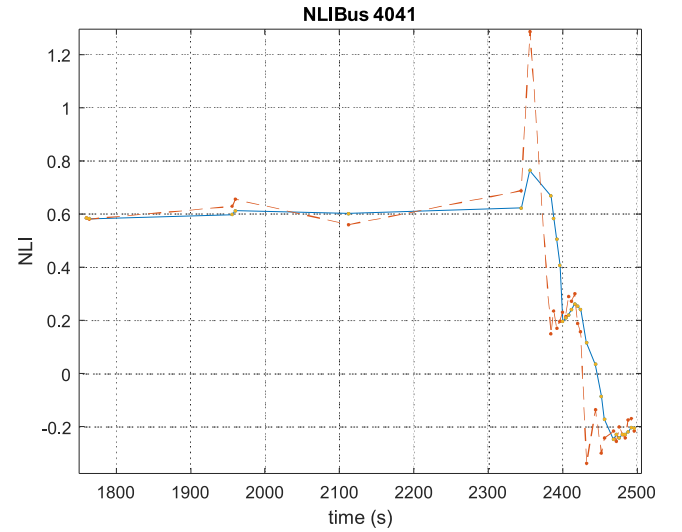Before the simulated disturbance of [16] which consists of a short-

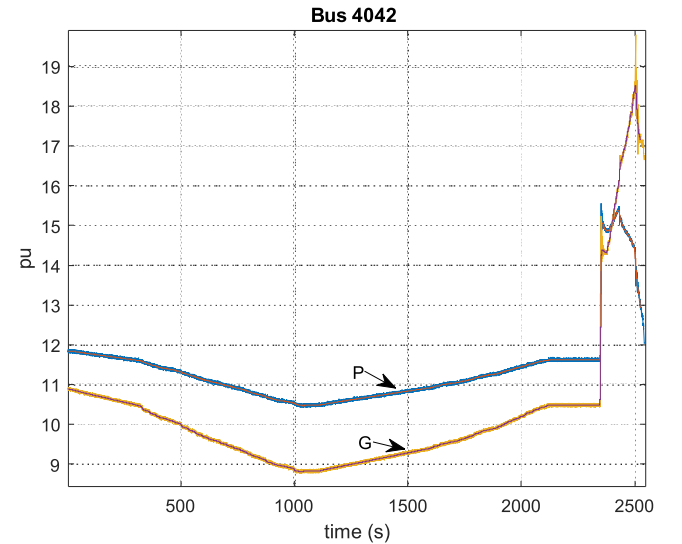**Fig. 11.** Bus 4041 $\overline{NLI}$ (blue) and NLI (dashed) time response (unstable case).

Fig. 12. Bus 4042 active power and apparent conductance during contingency (unstable case).
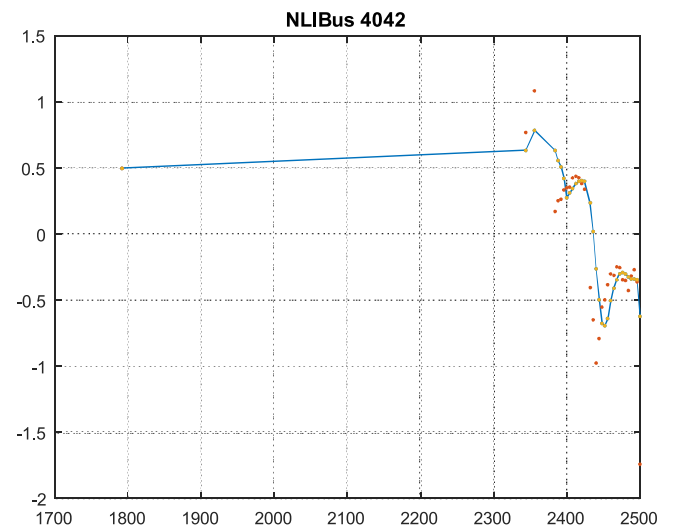

Fig. 13. Bus 4042 $\overline{NLI}$ (blue) and NLI (dotted) time responses (unstable case).
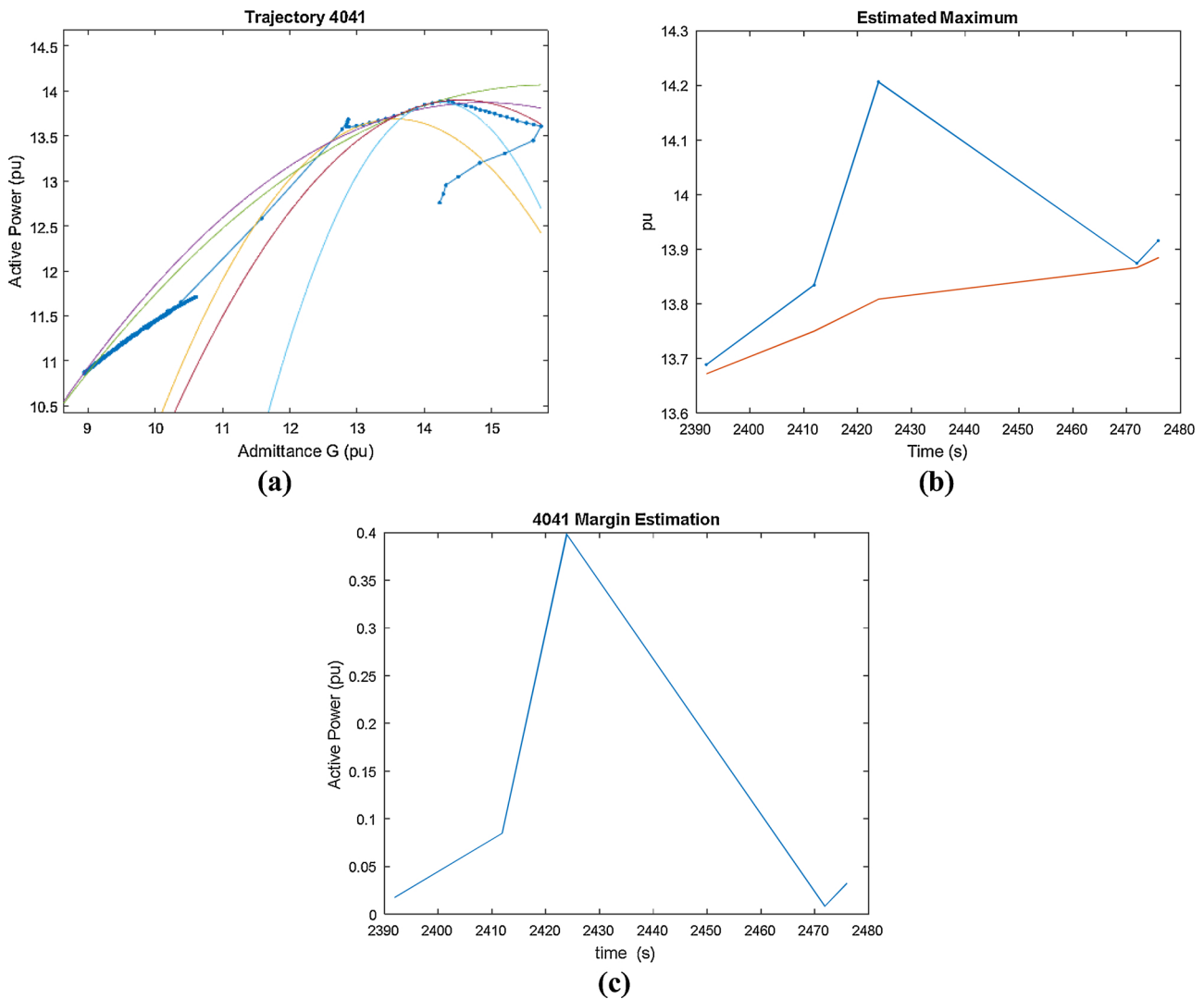
Fig. 14. (a) Bus 4041 filtered trajectory, (b) maximum power tracking and (c) margin estimation (unstable case).

circuit followed by a corridor line disconnection, in this paper two opposite load demand ramps are simulated to help initialize the *NLI* Index: First a load ramp-down followed by a ramp-up, each with ± 7% total variation lasting for 1000 s. During the second of these ramps the *NLI* is initialized at each boundary receiving bus as in an ordinary daily system operation. The net result of the two ramps is to bring back the system approximately to the same operating point as the initial one with the *NLI* values properly initialized. After the demand ramp-up is completed, a solid three-phase fault occurs at line 4032–4044 at the line end near bus 4032. The short-circuit is cleared after 100 ms and isolated through the line disconnection.

Bus 4044 is no longer a boundary bus after the line disconnection, since the remaining power flows arrive from the adjacent receiving end buses 4041 and 4042. Thus, bus 4044 will be excluded from stability monitoring. The downstream apparent load conductance increase is of course more complex in this case compared to the radial system presented in the previous Section, since each PMU calculates a conductance which represents a downstream power system area instead of an individual load, consisting of generator units, transmission lines, as well as lumped loads equipped with discrete LTC mechanisms.

6.2. Point A: unstable response

In the unstable scenario, the analysis focuses on the effectiveness of

the proposed method to estimate voltage stability margin prior to instability detection and thus provide an earlier indication of the incoming instability. *NLI* performance for instability onset identification has already been presented in [12]. The only difference is the time shift due to the two initial demand ramps.

In Fig. 9 the incoming active power and apparent conductance at receiving boundary bus 4041 is presented.

The contingency occurs at about 2300 s. It can be observed that during the initial ramps active power P_{4041} and apparent conductance G_{4041} exhibit a similar behaviour reflecting stable system response, where decreasing apparent conductance corresponds to decreasing active power demand and vice versa. This pattern does not hold, however, after the line disconnection as seen more clearly in Fig. 10, where the system response shortly before and after the line contingency is presented. As seen, line disconnection causes an abrupt change in both imported active power and apparent conductance. The resulting electromechanical oscillations die out after approximately 30 s. At about the same time the LTCs start to restore load at the Central Area. The received active power exhibits a transient local minimum approximately between $t = 2350\,s$ and $t = 2380\,s$ while the apparent conductance (reflecting downstream demand) increases slightly. This, however, does not raise an alarm due to the filtering aspects discussed in Section 2.3.
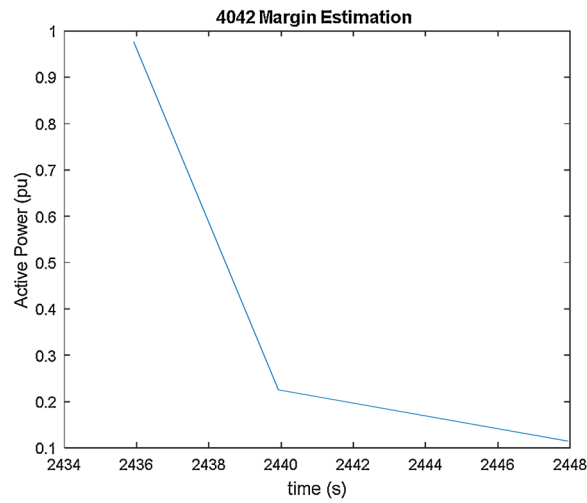
In Fig. 11 the evolutions of calculated *NLI* (dashed red line) and its
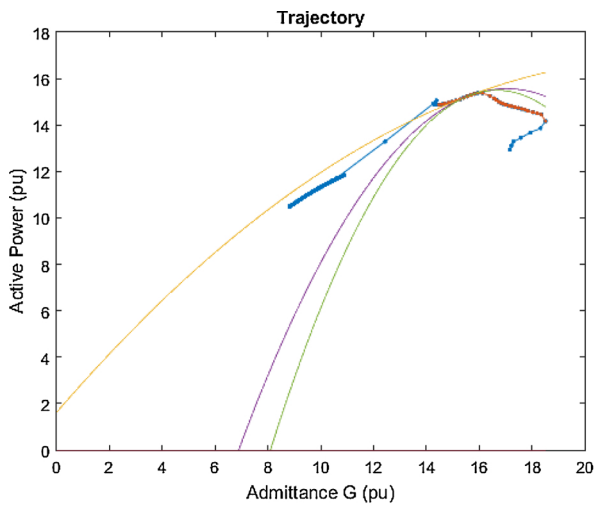
(a)
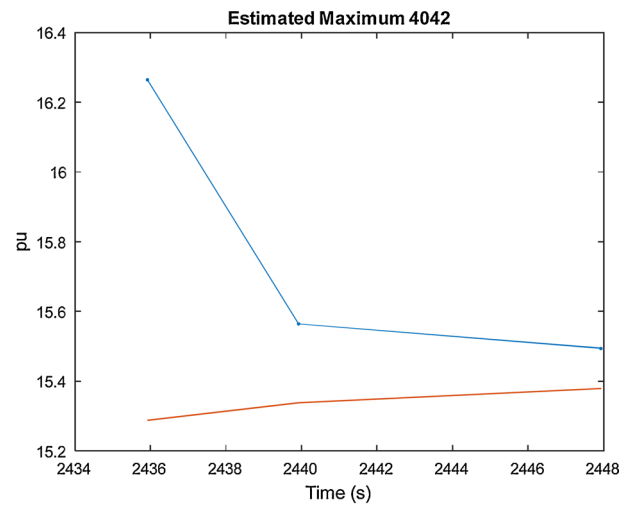
(b)

(c)

Fig. 15. (a) Bus 4042 filtered trajectory, (b) maximum power tracking and (c) margin estimation (unstable case).
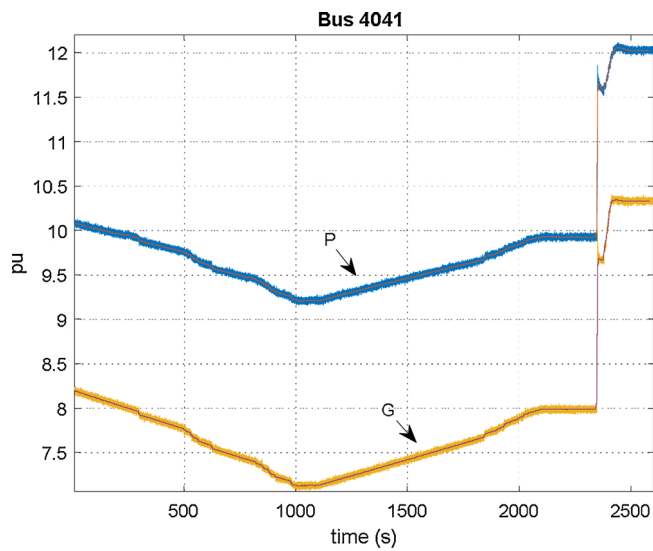

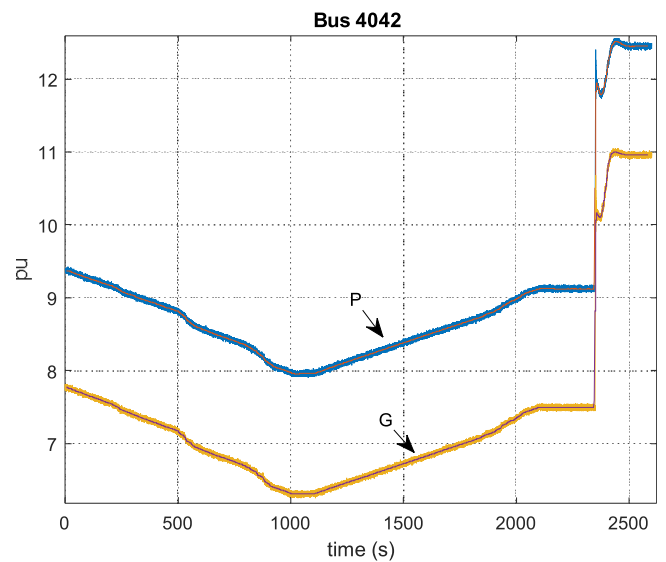**Fig. 16.** Bus 4041 active power and apparent conductance (stable case).

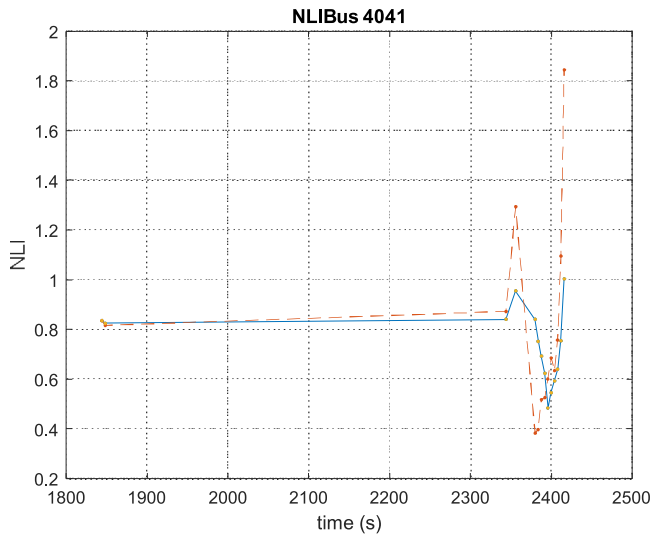**Fig. 17.** Bus 4042 active power and apparent conductance (stable case).

Fig. 18. Bus 4041 $\overline{NLI}$ and *NLI* time responses (stable case).
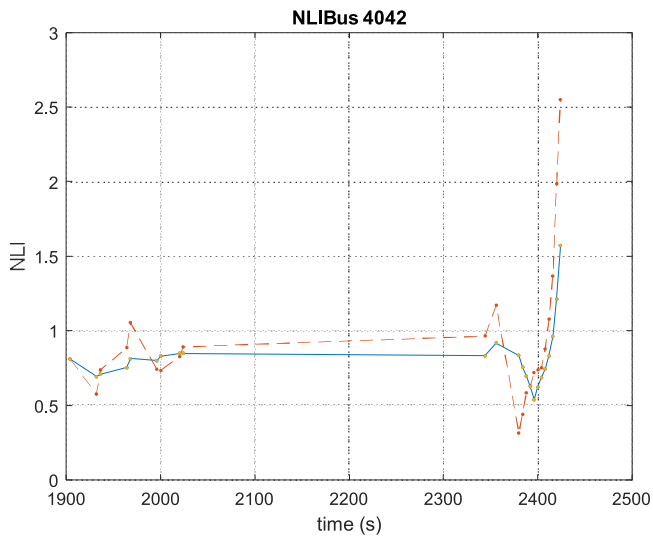

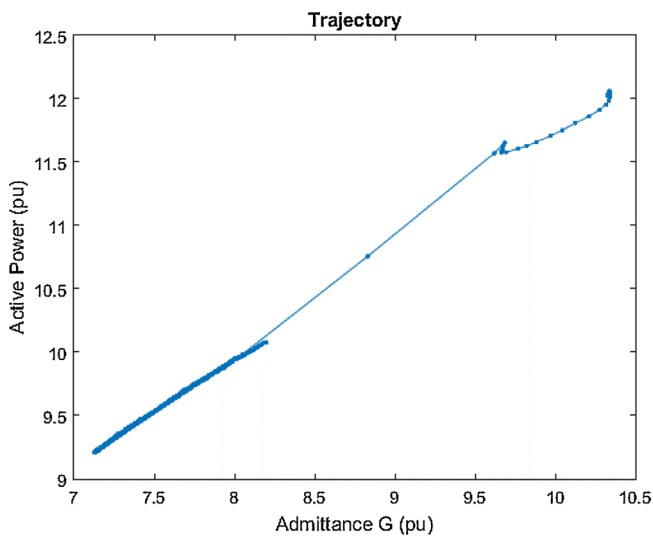**Fig. 19.** Bus 4042 $\overline{NLI}$ and *NLI* time responses (stable case).

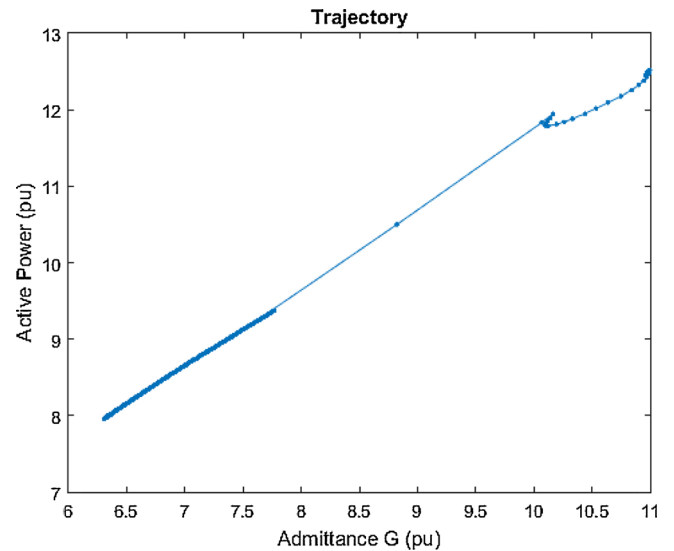**Fig. 20.** Bus 4041 filtered trajectory and maximum power tracking (stable case).

Fig. 21. Bus 4042 discrete trajectory and maximum power tracking (stable case).

averaged value $\overline{NLI}$ (blue line) at bus 4041 is depicted. One minute approximately after the disturbance, at simulation time $t = 2360\,s$, *NLI* values exhibit some fluctuations, after which a decreasing pattern appears at the average *NLI*. The moving average of the *NLI* becomes negative at time $t = 2445\,s$ approximately, indicating instability onset.

Figs. 12 and 13 depict the transmitted active power and apparent conductance, and the *NLI* values respectively for the receiving boundary bus 4042. As can be observed, the behaviour is quite similar to that for bus 4041, indicating that the Central Area demand cannot be restored due to the weakened system and corresponding reduced power transfer capability after the line disconnection.

In Fig. 14 (a) the trajectories in the $G - P$ space corresponding to the filtered values $P_{i,f}$ and $G_{i,f}$ for bus 4041 and the calculated interpolating polynomials are illustrated. It can be observed that in the $G - P$ space, the margin estimation method is able to identify that the system trajectory tends to reach a maximum power transfer point. In Fig. 14(a) one of the generated polynomials does not obtain a maximum value within the assumed operational window of apparent conductance G, since it tends to increase beyond the value $G = 20\,pu$.

In Fig. 14(b) it is seen that the first interpolating polynomial is calculated at around $t = 2390\,s$, e.g. approximately 40 s before the instability onset. This time window allows the option of performing automated preventive countermeasures such as emergency reactive power support. It should be mentioned that during the voltage instability incident the transmission system voltages in the corridor are above 1.0 pu, indicating no obvious voltage instability issue in the system.

Finally, in Fig. 14(c) the resultant voltage stability margin estimation is depicted as function of calculation time. It can be observed that although the evolution of the pattern is not as smooth as for the radial system in Figs. 4 or 7, a convergence between the estimated maximum value and the actual transferred active power can be observed, illustrating the validity of the proposed measurement-based method.

In Fig. 15 the same plots are drawn for bus 4042. In Fig. 15 (a) the trajectory and polynomials are drawn in the $G - P$ space, while in Fig. 15(b) the estimated maximum power and the actual transfer are shown. It is seen that the first estimate is achieved at $t = 2435\,s$, i.e. in less than 10 s before the receiving boundary bus imported active power attains its maximum value which causes the issue of an alarm. Clearly for this bus there is less advance warning for preventive measures and only corrective action after the issue of the alarm is possible. Finally, in Fig. 15(c) the reduced margin is shown as the system approaches maximum power transfer.

6.3. Point B: stable response

When the system is operating initially at point B, following the same sequence of disturbances the response of the system is stable. The same initialization ramps are simulated to initialize *NLI* prior to the contingency. The time responses of imported power *P* and apparent conductance *G* at the receiving boundary buses 4041 and 4042 are depicted in Figs. 16 and 17 respectively.

As seen, after the contingency occurring at time $t = 2300\,\text{s}$, the system reaches eventually a new long-term equilibrium, where the initial load demand is restored. A steep ramp-up is observed after the post-disturbance transient in both *P* and *G* time responses, resulting from the LTC dynamics leading to the establishment of a new long-term equilibrium point.

In Figs. 18 and 19 the evolutions of the *NLI* (dashed red line) and its corresponding averaged value *N̄LI* (blue line) for buses 4041 and 4042 respectively are depicted. It is observed that in both boundary buses the *NLI*s retain values far from zero, thus indicating sufficient voltage stability margin during the system response.

As seen in Figs. 18 and 19, the pre-contingency values of *NLI* for both boundary buses are higher for the secure operating point B with respect to the insecure operating point A. More specifically the *NLI* is 0.8 instead of 0.6 for bus 4041, and 0.9 instead of 0.5 for bus 4042. This shows a good correlation between pre-contingency *NLI* values and security margin, even though it is difficult to set an a priori security threshold for *N̄LI*, which for the specific system contingency would be close to 0.6.

In Figs. 20 and 21 the filtered trajectories of buses 4041 and 4042 on the $G - P$ space are presented. As can be observed, there is a discontinuity during the line contingency and the post-contingency trajectory settles at a final long-term equilibrium. No interpolating polynomials need to be calculated in this case, since the *NLI* values do not follow a descending pattern for consecutive calculations. The fact that no interpolating polynomials are calculated is another indication (apart from the higher pre-contingency *NLI* values) that the system is not prone to an imminent instability, thus there is no need to provide preventive countermeasures.

Overall the security of case B is demonstrated not only by the positive values of *NLI* after the disturbance (no alarm issued), but also by the higher pre-contingency *NLI* values and the fact that there was no need to compute stability margins.

7. Conclusions

In this paper two important issues relative to real-time voltage instability monitoring were addressed, namely the effect of active losses on the accuracy of maximum power estimation, and the possibility for a measurement based only voltage stability margin estimation.

For the first issue, the performance of the local measurement-based voltage stability Index *NLI* in a radial power system with losses was investigated and analytical expressions associated with maximum power transfer in the presence of losses were presented. It was shown that the *NLI* measured from a PMU placed at an intermediate transmission bus detects exactly the voltage instability onset in a radial lossless system, while it is slightly delayed in the presence of network losses. The degree of this delay was quantified in percentage of error made in the estimation of the load conductance corresponding to maximum power transfer. Further studies should be performed to establish the applicability of the *NLI* in actual system operation. A first step will involve post-mortem analysis of actual voltage collapse incidents, that can be replayed in simulation to determine the exact time at which the Index would identify the instability, if it were in operation. Also issues relative to measurement noise and filtering can be further investigated in the process of actual system application.

The second point addressed was the introduction of a measurement-based voltage stability margin estimation method. The method is based on the information provided by the *NLI* during a long-term evolution, in which *NLI* is progressively decreasing. The method does not rely on a network model and utilizes interpolating polynomials of the calculated active power and apparent conductance values measured at a transmission system bus.

Numerical results for a radial network with and without network losses and measurement noise verified the theoretical analysis presented in this paper and showed good performance of the *NLI*, as well as of the margin estimation method.

A second test case was run using the IEEE Nordic Test System with two operational scenarios, one resulting in voltage instability and one with stable response to the same simulated contingency. For the unstable scenario it was observed that the margin estimation method provides a number of stability margin calculations prior to the instability alarm issued by the *NLI*. The stability margin calculations however are quite close to the alarm, so the time window left is sufficient only for automatic preventive control actions. In the stable scenario, conditions for stability margin calculation were not met, reflecting a stable system response with no voltage instability indications.

Further research can focus on utilizing other means of calculating the estimated maximum power at the receiving boundary buses of an area prone to long-term voltage instability, such as regression techniques. Furthermore, a case study on a real-world power system is deemed appropriate for assessing the performance of the presented topics in the paper in realistic case. It is also mentioned that some polynomials tend to attain their maximum values at an apparent conductance which is considerably larger than the one in which they are calculated and can thus be considered as inaccurate and could be excluded, so as to avoid large deviations on the margin estimations. Further research on this topic is also necessary.

Declaration of Competing Interest

The authors declare that they have no known competing financial interests or personal relationships that could have appeared to influence the work reported in this paper.

References

[1] C.W. Taylor, Power System Voltage Stability, McGraw-Hill Education, New York, 1994.
[2] T. Van Cutsem, C. Vournas, Voltage Stability of Electric Power Systems, Springer, 2008.
[3] P. Kundur, C.W. Taylor (Chair), IEEE Task Force on Blackout Experience, Mitigation, and role of new technologies, IEEE/PES Task Force, Power System Dynamic Performance Committee, PES, 2007.
[4] M. Glavic, T. Van Cutsem, Wide-area detection of voltage instability from synchronized phasor measurements. Part I: principle, IEEE Trans. Power Syst. 24 (August (3)) (2009) 1408–1416.
[5] Mevludin Glavic, Thierry Van Cutsem, Wide-area detection of voltage instability from synchronized phasor measurements. Part II: simulation results, IEEE Trans. Power Syst. 24 (August (3)) (2009) 1417–1425.
[6] K. Vu, M. Begovic, D. Novosel, M.M. Saha, Use of local measurements to estimate voltage-stability margin, IEEE Transactions Power Syst. 14 (August (3)) (1999) 1029–1035.
[7] S. Corsi, G.N. Taranto, A real-time voltage instability identification algorithm based on local phasor measurements, IEEE Trans. Power Systems 23 (August (3)) (2008) 1271–1279.
[8] Y. Wang, et al., Voltage stability monitoring based on the concept of coupled single-port circuit, IEEE Trans. Power Syst. 26 (November (4)) (2011) 2154–2163.
[9] C.D. Vournas, N.G. Sakellaridis, Tracking maximum loadability conditions in power systems, Proc. of 2007 IEEE iREP Symposium - Bulk Power System Dynamics and Control VII: Revitalizing Operational Reliability, Charleston, SC, USA, December, 2007.
[10] F. Hu, K. Sun, A.D. Rosso, E. Farantatos, N. Bhatt, Measurement-based real-time voltage stability monitoring for load areas, IEEE Trans. Power Syst. 31 (July (4)) (2016) 2787–2798.
[11] L. Ramirez, I. Dobson, Monitoring Voltage Collapse Margin by measuring the area voltage across several transmission lines with synchrophasors, IEEE PES General Meeting, National Harbor MD USA, July, 2014.
[12] C.D. Vournas, C. Lambrou, P. Mandoulidis, Voltage Stability Monitoring from a Transmission Bus PMU, IEEE Trans. Power Systems vol. 32, (no. 4) (2017) 3266–3274.
[13] M. Begovic, A. Peerzada, R. Nuqui, B. Picone, Locational Accuracy of VIP Indices for

Voltage Collapse Margin Estimation, 51st Hawaii International Conference on System Sciences (2018) January.

[14] C.D. Vournas, P. Mandoulidis, On-Line Voltage Stability Monitoring, Proceeding of IEEE International Symposium on Circuits & Systems, Florence May, 2018.

[15] L. Burdain, J.D. Faires, A.M. Burdain, Numerical Analysis, Cengage Learning, (2016).

[16] T. Van Cutsem, Test systems for votage stability analysis and security assessment, PES Technical Report PES-TR19, IEEE/PES Task Force, Power System Dynamic Performance Committee, 2015 August. [Online]. Available: http://resourcecenter. ieee-pes.org/pes/product/technical-reports/PESTR19.

[17] P. Aristidou, D. Fabozzi, T. Van Cutsem, Dynamic simulation of large-scale power systems using a parallel schur-complement-based decomposition method, IEEE Trans. Parallel Distrib. Syst 25 (October (10)) (2014) 2561–2570.